# research papers

# Sub-microsecond-resolved multi-speckle X-ray photon correlation spectroscopy with a pixel array detector

Qingteng Zhang,[a] Eric M. Dufresne,[a] Suresh Narayanan,[a] Piotr Maj,[b] Anna Koziol,[b] Robert Szczygiel,[b] Pawel Grybos,[b] Mark Sutton[c] and Alec R. Sandy[a]*

[a]X-ray Science Division, Argonne National Laboratory, 9700 South Cass Avenue, Lemont, IL 60439, USA, [b]AGH University of Science and Technology, al. Mickiewicza 30, Krakow 30-059, Poland, and [c]Department of Physics, McGill University, 3600 Rue University, Montréal, QC, Canada H3A 2T8. *Correspondence e-mail: asandy@anl.gov

Small-angle X-ray photon correlation spectroscopy (XPCS) measurements spanning delay times from 826 ns to 52.8 s were performed using a photon-counting pixel array detector with a dynamic range of 0–3 (2 bits). Fine resolution and a wide dynamic range of time scales was achieved by combining two modes of operation of the detector: (i) continuous mode, where data acquisition and data readout are performed in parallel with a frame acquisition time of 19.36 µs, and (ii) burst mode, where 12 frames are acquired with frame integration times of either 2.56 µs frame$^{-1}$ or 826 ns frame$^{-1}$ followed by 3.49 ms or 1.16 ms, respectively, for readout. The applicability of the detector for performing multi-speckle XPCS was demonstrated by measuring the Brownian dynamics of 10 nm-radius gold and 57 nm-radius silica colloids in water at room temperature. In addition, the capability of the detector to faithfully record one- and two-photon counts was examined by comparing the statistical distribution of photon counts with expected probabilities from the negative binomial distribution. It was found that in burst mode the ratio of 2 s to 1 s is markedly smaller than predicted and that this is attributable to pixel-response dead-time.

## 1. Introduction

The implementation of multi-bend achromat (MBA) lattices in new and existing synchrotron-based X-ray sources (e.g. Eriksson et al., 2014) will provide large increases in time-average coherent flux and promises even more dramatic gains in the time resolution of X-ray photon correlation spectroscopy (XPCS) measurements since minimum accessible delay times scale with the square of the coherent flux (Jakeman, 1973; Falus et al., 2006). To achieve the promised gains in time resolution, however, corresponding developments are required in high-speed high-fidelity XPCS-relevant area detectors. For XPCS, area detectors have demonstrated considerable gains over point detectors because they span a range of reciprocal space enabling so-called multi-speckle XPCS with improved signal-to-noise ratio (SNR) for the same radiation dose (Dierker et al., 1995; Lumma et al., 2000; Falus et al., 2006; Leitner et al., 2009; Vodnala et al., 2018; Verwohlt et al., 2018), direction-sensitive studies (Livet et al., 2006; Fluerasu et al., 2008; Burghardt et al., 2012; Shinohara et al., 2013; Rogers et al., 2014; Wandersman et al., 2015; Nygård et al., 2016; Lhermitte et al., 2017) and the measurement of two-time correlation functions that provide information about
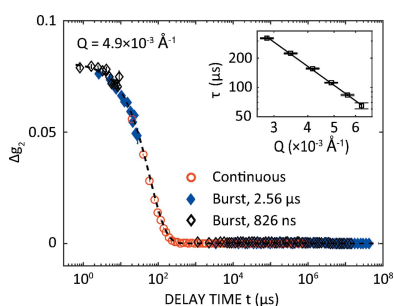
intermittent dynamics and fluctuations away from equilibrium conditions (Malik *et al.*, 1998; Sutton *et al.*, 2003; Sanborn *et al.*, 2011; Müller *et al.*, 2011; Orsi *et al.*, 2012; Evenson *et al.*, 2015). In recent years, photon-counting pixel array detectors (PADs) have emerged as powerful tools for a number of X-ray scattering techniques because of their ability to faithfully record wide-dynamic-range signals at synchrotrons, their absence of readout noise and dark currents, their narrow point-spread response, large collection areas and relative ease of use (*e.g.* Broennimann *et al.*, 2006; Kraft *et al.*, 2009). Such detectors have also found application in XPCS measurements because of their increasingly fast continuous frame rates and relatively small pixel sizes (Johnson *et al.*, 2012; Westermeier *et al.*, 2016; Zhang *et al.*, 2016). Comparing frame rates across different detectors, though an important metric for XPCS, is not so straightforward because of varying sensor sizes, bit depths and 'continuous' acquisition times that often, in practice, require pauses for moving data from one location to another. Within these qualifiers, however, the fastest continuous frame rate for XPCS-suitable PADs is currently about 50 kHz (Zhang *et al.*, 2017). One way to significantly increase the frame rate is using a so-called burst mode that takes frames at very high speed by using memory local to a pixel to store a typically small number of frames before a slower readout. Several X-ray detectors using this mode of operation have been developed recently (Becker *et al.*, 2011, 2013; Schwandt *et al.*, 2013; Philipp *et al.*, 2016). To date, these detectors are targeted towards X-ray free-electron laser applications and have limited potential usefulness for XPCS at storage-ring-based light sources because of their relatively large pixels and, more significantly, because the time scales provided during the burst, and the repeat between bursts, do not overlap yielding gaps in the desired continuous spectrum of XPCS delay times.

Here we present the use of the ultrafast X-ray camera (UFXC32k) (Grybos *et al.*, 2016; Koziol *et al.*, 2018) previously used for XPCS in a continuous measurement mode up to 50 kHz (Zhang *et al.*, 2017), in both burst and continuous modes to provide access to XPCS delay times from 826 ns to 52.8 s. In burst mode, the detector acquires 12 frames at one of two frame rates: 390 kHz (for 31 µs) or 1.2 MHz (for 9.9 µs). We demonstrate the applicability of this detector for XPCS by measuring the Brownian dynamics of 10 nm-radius gold and 57 nm-radius silica nanoparticles in water. We also assess the ability of the detector to record scattered X-rays with high fidelity by analyzing the statistical distribution of one- and two-photon counts (1 s and 2 s) in a pixel within single-frame exposure times, $t_e$, of 2.56 and 19.36 µs. We compare the measured distribution of counts with expectations for scattering with a partially coherent X-ray beam and find that for the burst-mode measurements the ratio of 2 s to 1 s is significantly less than expected. We show that this difference is attributable to pixel-response dead-time, $\tau_D$. The remainder of this paper is organized as follows: §2 summarizes the instrumentation, §3 discusses small-angle X-ray scattering (SAXS) and XPCS measurements made with the UFXC32k, §4 examines the distribution of photon counts recorded by the detector, and §5 concludes.

## 2. Instrumentation

The UFXC32k detector is a dual-counter photon-counting PAD comprising $128 \times 256$ 75 µm-square pixels. The sensor layer is silicon and is 320 µm thick. Technical details regarding the sensor design and the digitizing electronics have been published previously (Grybos *et al.*, 2016; Koziol & Maj, 2018). The detector control unit (DCU) is implemented using the National Instruments (NI) 7935 FlexRIO system equipped with the Kintex-7 xc7k410t FPGA, 2 GB of DRAM and an NI 6589 adapter module and was programmed using *LabVIEW*. The DCU implements both burst and continuous modes of operation; switching between modes is performed in the software. To achieve the highest frame rates, the dynamic range is set to 2-bits (0–3) for both modes of operation. With a 2-bit dynamic range, the frame rate in both continuous and burst modes depends only on the frequency of the clock signal sent to the detector by the DCU, so the faster the clock rate, the faster the frame rate. For our measurements the clock rate was set to 440 MHz in continuous mode and 310 MHz or 100 MHz in burst mode during 1.2 MHz or 390 kHz frame acquisition, respectively.

Another feature in the control system is data sparsification. Before the FPGA sends the frames accumulated inside DRAM memory to the DCU, it sparsifies the data. The sparsification algorithm sends only the addresses of pixels that were hit together with their counter values and the frame number in the data acquisition sequence. This approach produces smaller per-frame data sets allowing more frames to be collected before pausing and also makes the entire data acquisition pipeline faster than it would be otherwise. Lastly, we note that the continuous frame rate of nearly 52 kHz is considerably higher than the 11.8 kHz frame rate that was reported recently for the same detector system (Zhang *et al.*, 2016). The key feature that allowed the system to operate at higher frame rates in continuous mode was an upgrade of the DCU that now allows the digital communication to operate at considerably higher speeds.

In continuous mode, as illustrated in Fig. 1(*a*), the detector operates at a frame rate of 51.67 kHz, *i.e.* an exposure time of 19.36 µs, for the largest number of frames that can be accumulated in the DCU before acquisition is paused and the frames read out and transferred to a device with more storage. During this mode, each pixel is connected to two counters that are configured to alternately accumulate photon hits and then be read out, largely eliminating exposure dead-time; *i.e.* during one 19.36 µs exposure, counter 2 is accumulating X-ray counts while counter 1 is read out within this period, whereas in the next 19.36 µs exposure counter 1 is accumulating X-ray counts while counter 2 is being read out, and so on. The minimum delay time in this mode is the frame spacing of 19.36 µs while the longest delay time depends on a combination of the 2 GB of DRAM accessible by the FPGA and the signal level since the data are sparsified. For our measurement conditions this was a little over 3.87 s (200000 frames).

In burst mode, as illustrated in Fig. 1(*b*), the detector acquires 12 frames and stores the counts in the two 14-bit
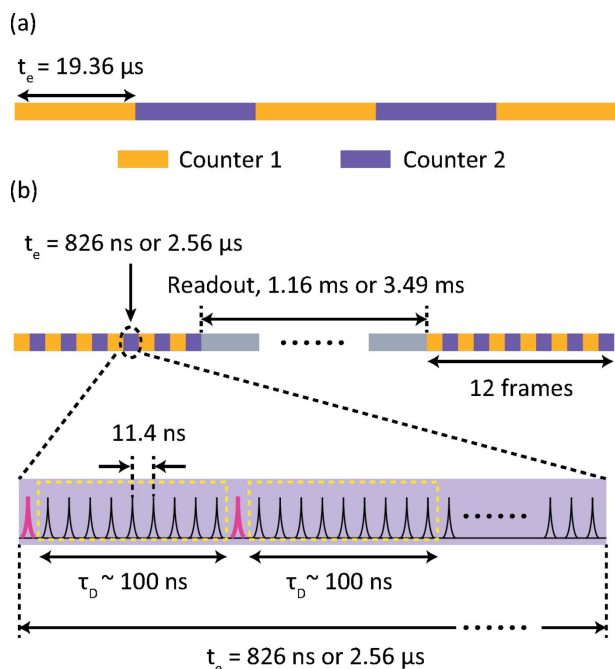
**Figure 1**
Illustration of the timing structures for (*a*) continuous- and (*b*) burst-mode acquisition. In continuous mode, the two counters per pixel alternate between accumulating events and being read out. In burst mode, the counts in 12× short exposures are stored in the pixel-local counters before a longer interval is used to read out the stored data. The schematic below (*b*) illustrates pixel-response dead-time and its effect on recording multiple photons in a single exposure.

counters that are integral to each pixel before a longer pause during which the frames stored in the counters are moved to the DCU. Following this, the next burst is acquired. This process can be repeated until the DCU memory is filled and acquisition is paused for a longer period while the frames are transferred to another storage device. We tested this mode at two frame rates: the first, 390 kHz, provided an exposure time of 2.56 µs with a gap between bursts of 3.49 ms, while the second, 1.2 MHz, provided an exposure time of 826 ns with a gap between bursts of 1.16 ms. For the measurement conditions in this manuscript, the maximum number of frames acquired during either burst mode was 180000. As illustrated in Fig. 1(*b*), the longest delay time achieved during a 390 kHz burst is $11 \times 2.56 = 28.16$ µs and this exceeds the shortest delay time in continuous mode. Moreover, the longest delay time achieved during a 1.2 MHz burst is $11 \times 0.826 = 9.1$ µs and this exceeds the shortest delay time in the 390 kHz burst mode. The combination of three exposure times using burst and continuous modes provides a gap-free measurement of delay times spanning 826 ns to 52.8 s. In the remainder of this document we refer to the combination of burst- and continuous-mode measurements as hybrid-mode measurements.

## 3. SAXS and XPCS

We evaluated the detector's ability to perform hybrid-mode XPCS measurements by making time-resolved coherent SAXS measurements, *i.e.* SA-XPCS measurements, at beam-line 8-ID-I at the Advanced Photon Source (APS). The measurements were made in 324-bunch non-top-up mode operation of the storage ring. In this mode, the time between X-ray pulses is 11.4 ns, the bunch currents are uniform and they vary smoothly from 0.32 to 0.26 mA per bunch over the course of each 12 h fill. One benefit of this mode is the uniform current per bunch that eliminates aliasing effects that could appear in burst-mode data from the uneven distribution of bunch currents during the APS's more typical 24-bunch top-up operation since the storage ring revolution time of 3.682 µs is longer than the burst-mode exposures of 826 ns or 2.56 µs. A drawback is that the bunch separation is considerably less than the pixel-response dead-time, $\tau_D$ (Walko *et al.*, 2008), that we estimate is 130 ns (see below). As we will discuss later, $\tau_D$ affects the detector's ability to faithfully record two (or more) one-photon hits in a pixel in a frame and this issue, especially during burst exposures, noticeably impacts determination of the speckle-pattern contrast *via* statistical distribution methods (Hruszkewycz *et al.*, 2012; Inoue *et al.*, 2012; Li *et al.*, 2014; Verwohlt *et al.*, 2018). This issue, however, has a negligible effect on average intensity measurements or time-series XPCS measurements provided that the characteristic sample fluctuation times are long compared with $\tau_D$ and the per-pixel signal rates are well below $1/\tau_D$ (Schätzel, 1986); both of these conditions are satisfied for the measurements presented below (Figs. 2–5).

The X-ray beam was generated by tandem 33 mm-period, 2.4 m-long undulators. A plane silicon mirror at a deflection angle of 5 mrad was used to filter out higher harmonics and a Ge(111) monochromator with a relative bandpass of 0.03% full width at half-maximum (FWHM) selected a 10.91 keV X-ray beam. A 180 µm vertical portion of the incident beam (approximately the vertical coherence length at the position of the focusing optic) was focused 2 m downstream to a FWHM at the sample position of 2 µm using Be compound refractive lenses. In the horizontal direction, a 20 µm horizontal colli-mating slit selected a few horizontal coherence lengths of the incident beam. The partially coherent flux at the sample position was $3.8 \times 10^{10}$ photons s$^{-1}$. Three guard slits between the beam-defining slits and the sample were used to reduce parasitic scattering. The detector was placed 4 m downstream of the sample and a tungsten beamstop immediately upstream of the detector blocked the transmitted direct beam.

We performed SA-XPCS measurements of citrate-capped spherical gold nanoparticles dispersed in water at a volume fraction of 0.026% and silica nanoparticles dispersed in water at a volume fraction of 2.5%. All measurements were made at room temperature. For the gold nanoparticles, the sample was contained in a 1.5 mm-diameter quartz capillary. For the silica nanoparticles, the sample was sealed in an aluminium cell with Kapton windows for X-ray access. The sample thickness along the X-ray beam is 1.5 mm. Fig. 2 shows the 2D scattering from the gold nanoparticle sample: Fig. 2(*a*) shows the time average of 20000 frames collected in continuous mode (0.39 s of counting time) while Fig. 2(*b*) is the average of 30000 frames collected in 2.56 µs burst mode (8.702 s = 0.077 s of counting time and 8.625 s of counter readout). The *x* and *y* axes are in
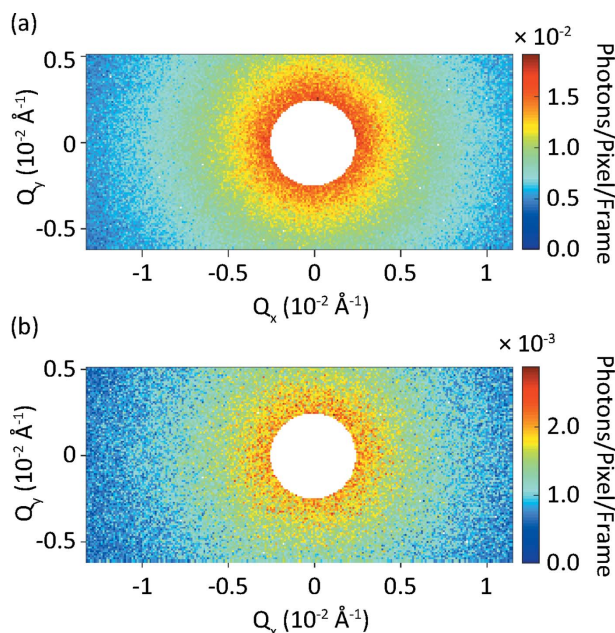
**Figure 2**
Time-average 2D SAXS patterns acquired from the gold nanoparticle suspensions using (*a*) continuous- and (*b*) 2.56 µs burst-mode operation of the detector. The white circle in the center of each image is the shadow of the beam stop that has been masked out of the analysis while isolated white pixels are blemishes that have also been masked out.

units of $Q$ where $Q = 2k\sin(2\theta/2)$ is the wavevector transfer, $k = 2\pi/\lambda$ is the wavevector, $\lambda$ is the X-ray wavelength and $2\theta$ is the scattering angle.

Fig. 3 shows the 1D SAXS results for the gold and silica nanoparticle suspensions obtained by azimuthally averaging the 2D scattering intensities like those shown in Fig. 2 around the origin of reciprocal space. The intensities are plotted *versus* scaled wavevector $QR$ where $R$ are the fitted radii of the different nanoparticle suspensions. Open and closed symbols are gold suspension continuous- and burst-mode data,
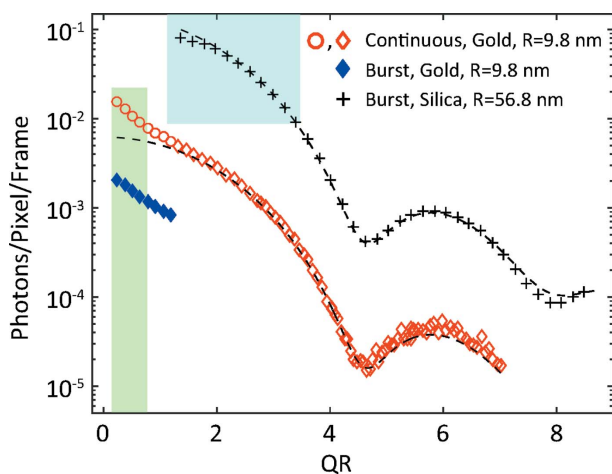
respectively, while plus symbols are data from the silica suspension. The gold continuous-mode results were collected at five detector positions to span a larger range of reciprocal space, but because of intensity limitations the XPCS analysis was confined to the smallest $Q$ values shown by the green shaded rectangle in Fig. 3. The difference in intensities between the continuous- and burst-mode gold data is the ratio of exposure times while the intensities from the silica suspension are higher because of the larger particle size and concentration. The nanoparticle sizes can be estimated by fitting the data to a model comprising spherical particles having a Gaussian size distribution (Rieker *et al.*, 1999). For gold, reasonable agreement is found between the experimental results and the form factor for spheres with a mean radius of 9.8 nm and a standard deviation of 0.8 nm (black dashed line). The discrepancy at smaller $Q$ likely arises from some aggregation of the gold nanoparticles which might have occurred because the sample was not measured for a long time after it was purchased from the vendor. For silica, the same analysis yields a mean nanoparticle radius of 56.8 nm and a standard deviation of 4.8 nm.

The $Q$-dependent intensity autocorrelation functions, $g_2(Q, t)$, of the nanoparticle suspensions are calculated according to

$$g_2(Q, t) = \frac{\left\langle \langle I_{i,j}(t') \, I_{i,j}(t' + t)\rangle_{t'}\right\rangle_{i,j}}{\left\langle \langle I_{i,j}(t')\rangle_{t'}\right\rangle_{i,j} \left\langle \langle I_{i,j}(t' + t)\rangle_{t'+t}\right\rangle_{i,j}}, \quad (1)$$

where $t$ is the delay time, and $I_{i,j}(t')$ and $I_{i,j}(t + t')$ are the scattering intensities at pixel $(i, j)$ collected at times $t'$ and $t + t'$, respectively. As discussed previously (Wong & Wiltzius, 1993; Dierker *et al.*, 1995; Cipelletti & Weitz, 1999; Lumma *et al.*, 2000) and reflected in equation (1), the correlations (numerator) are computed on a pixel-by-pixel basis first and then can be averaged within annuli of nominally equivalent $Q$ values to obtain improved signal. This approach also has the virtue of allowing the speckle contrast to be determined in a time series even if the sample is static (Lumma *et al.*, 2000). The correlations in the numerator are computed using the so-called multi-tau algorithm (Schätzel, 1990, 1993; Cipelletti & Weitz, 1999; Magatti & Ferri, 2001) yielding logarithmically spaced delay times. The averages in the denominator are calculated using smoothed symmetric normalization (Lumma *et al.*, 2000). The pixel averages $\langle \ldots \rangle_{i,j}$ were performed over pixels that fall within a range of $Q$ approximately one pixel wide ($1.0 \times 10^{-4}\ \text{Å}^{-1}$) to eliminate the effect of intensity variations with $Q$ on $g_2$. The $g_2(Q, t)$ values are further binned by a factor of ten in $Q$ to improve the SNR with the error bars approximated by the standard deviation of the $g_2$ values calculated for each pixel within each $Q$ bin.

To calculate $g_2$ for data acquired in hybrid mode, up to five time scales must be managed. Burst-mode data provide 2.56 µs- and 3.52 ms-resolution (3.49 ms + 12 × 2.56 µs, solid diamonds in Figs. 4 and 5) and 826 ns- and 1.17 ms-resolution (1.16 ms + 12 × 0.826 µs, empty diamonds in Fig. 5) results and $g_2$ for data acquired in each of these modes is calculated using the framework developed for kinetics-mode area-detector



**Figure 3**
SAXS intensity from continuous and 2.56 µs burst modes *versus* the scaled wavevector transfer $QR$. Dashed lines are fit results described in the text. Shaded regions indicate the ranges where the intensity autocorrelation functions displayed in Figs. 4 and 5 have been calculated.

Qingteng Zhang *et al.* • Sub-microsecond-resolved multi-speckle XPCS **1411**

XPCS data (Lumma *et al.*, 2000). Continuous-mode data provide 19.36 μs-resolution results (open circles in Figs. 4 and 5). The $g_2$ values from the burst and continuous modes are merged to produce $g_2$ values like those presented in Figs. 4 and 5.

Fig. 4 shows $\Delta g_2 = g_2 - 1$ plotted *versus* the delay time for $Q = 0.0042$ Å$^{-1}$. The 2.56 μs burst-mode measurements contain 30000 frames and were repeated 800 times to improve the SNR, while continuous-mode measurements contain 20000 frames and were repeated 200 times. The burst-mode results become increasingly noisy at larger delay times within each burst sequence because there are increasingly fewer intensity pairs to correlate. Nevertheless, there is good overlap with the continuous-mode data, and for correlation function fitting we can exclude the noisiest burst-mode data and use just the continuous-mode data.

As shown by the fit result (black dashed line) in Fig. 4, $\Delta g_2(Q, t)$ is well described using a $Q$-dependent exponential decay,

$$\Delta g_2(Q, t) = \beta_1 \exp\left[-2t/\tau(Q)\right], \tag{2}$$

where $\beta_1$ is the amplitude of the correlation function in the limit $t \to 0$ and reflects instrumental effects like the coherence of the beam relative to beamline aperture sizes and the pixel size of the detector, and $\tau(Q)$ is the $Q$-dependent correlation decay time. For simple diffusion anticipated for a dilute solution of spherical nanoparticles, $\tau(Q) = 1/(D_0 Q^2)$, where $D_0 = k_B T/(6\pi\eta R)$ is the diffusion coefficient, $k_B$ is Boltzmann's constant, $T$ is the temperature, $\eta$ is the viscosity and $R$ is the particle radius. Open squares in the inset show the fitted values of $\tau$ *versus* $Q$ and the solid line is a fit to these data with the slope fixed at $-2$. The slope was fixed to $-2$ because the $Q$-range of our measurements is not sufficient to enable more quantitative analysis (and because there is no reason to believe that the slope should not be $-2$ for the relatively dilute suspension that we studied). Evidently, our results are consistent with the nanoparticles exhibiting simple Brownian diffusion. Given the evidence for aggregation seen at small $Q$ in Fig. 3, we calculated the radius of gyration of the gold nanoparticle suspension from the fitted line using $\eta = 8.9 \times 10^{-4}$ Pa s$^{-1}$ (the viscosity of water at room temperature) and find $R = 19.9$ nm. This is a factor of two larger than the SAXS results. In this same vein, we note that from the vendor we know that the gold nanoparticles have a ~2 nm-thick citrate capping layer (that is largely invisible to SAXS) so, with regards to diffusion, even un-aggregated gold particles would have a hydrodynamic radius of 11.8 nm. Ultimately, these discrepancies reflect the fact that SAXS and XPCS are sensitive to different things: SAXS sees the size of the gold in the nanoparticles (and some aggregation of the gold) while XPCS sees the diffusion of the suspension which depends on the particle hydrodynamic radius and aggregation.

Fig. 5 presents results like those discussed above but for the 57 nm-radius silica nanoparticles. The particles scatter more and the diffusion is slower so the quality of the measured correlation function is much higher. Both the 826 ns and 2.56 μs measurements contain 180000 frames and were repe-

ated 100 and 13 times, respectively, to improve the SNR while continuous-mode measurements contain 50000 frames and were repeated 20 times. The inset to Fig. 5 shows the fitted results for $\tau(Q)$ (open squares) with a line of slope equal to $-2$ fitted to the points. The particle radius is determined as described above and yields $R = 64.8$ nm. This is 14% larger than the radius determined from SAXS.

As discussed above, the error bars on $g_2$ determined *via* the variance of $g_2$ within nominally equivalent $Q$ bands and plotted in Figs. 4 and 5 are quite different because of the large difference in scattering signals among other factors. Under assumptions applicable to our measurements the expected SNR for a measurement of $g_2$ has previously been shown to be (Falus *et al.*, 2006)

$$\mathrm{SNR}_{g_2} = \beta_1 \langle I \rangle \, t_e \left(N_f \, N_p\right)^{1/2}. \tag{3}$$
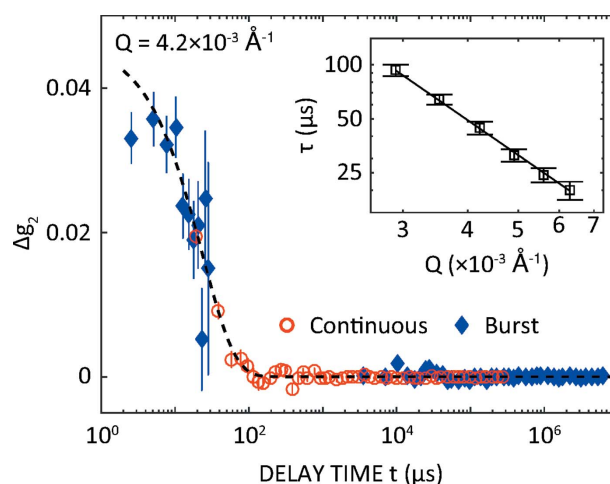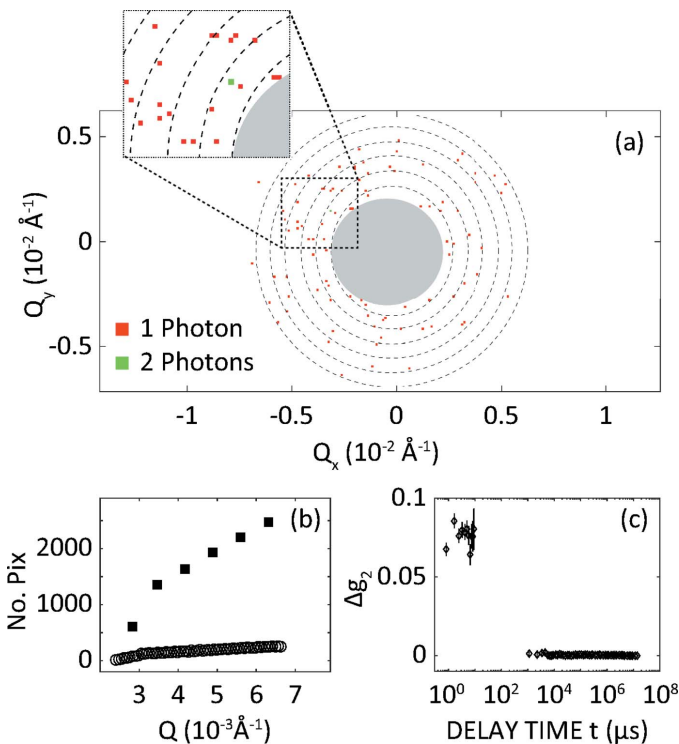
**Figure 4**
Time autocorrelation determined for gold suspension hybrid-mode data. The dashed line is a fit as described in the text. The inset shows $\tau$ *versus* $Q$ (open squares) and the solid line is a fit with the slope set to $-2$.
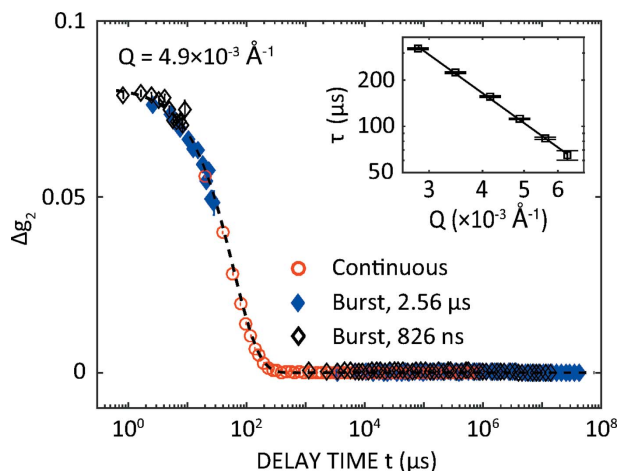
**Figure 5**
Time autocorrelation determined for silica suspension hybrid-mode data. The dashed line is a fit as described in the text. The inset shows $\tau$ *versus* $Q$ (open squares) and the solid line is a fit with the slope set to $-2$.

$\langle I \rangle$ is the average count rate per pixel, $t_e$ the exposure time, $N_f$ the number of frames (measurement time), and $N_p$ the number of pixels in the time and pixel averages in equation (1). It can be seen that the quality with which $g_2$ is measured can be improved, for example, by acquiring more frames (measuring longer) or with more coherent flux.

Equation (3) also demonstrates the power of multi-speckle XPCS since the SNR increases with the square root of the number of equivalent measurements (pixels). Fig. 6(a) shows the signal in a single frame from the 57 nm-radius silica suspension acquired during 1.2 MHz burst-mode operation. The gray circle is the masked-out shadow of the direct-beam stop, the dashed circles are the dynamic $Q$ partitions and the red and green dots are pixels that registered one or two photon counts, respectively, in the frame. This figure emphasizes how sparse the acquired data are, but, because many signals are acquired in parallel, high-quality correlation functions like those shown in Figs. 4 and 5 are obtained. For reference, Fig. 6(b) shows the number of pixels contributing to the static (open circles) and dynamic (solid squares) $Q$ partitions as discussed relative to equation (1). Lastly, though the $g_2$ SNR can be improved by repeating and averaging the same measurement, Fig. 6(c) shows that even a single 826 ns burst sequence of 180000 frames acquired from the 57 nm-radius silica suspension (0.15 s of signal measurement) yields $g_2$ with sufficient accuracy to distinguish the short-time amplitude of $g_2$ from the long-time baseline.



**Figure 6**
1.2 MHz burst-mode data acquired from the 57 nm-radius silica suspension. (a) A single frame showing the sparsity of the signal. (b) Number of equivalent pixels in the static (open circles) and dynamic (solid squares) partitions. (c) $\Delta g_2$ calculated from one burst-mode acquisition sequence of 180000 frames.

## 4. Photon counts distribution

The average count rates per pixel are low because of the combination of selecting a partially coherent X-ray beam from a third-generation synchrotron, short exposure times and the relatively dilute suspensions of small particles. On the one hand, this means that a 2-bit counter per pixel is sufficient for our measurements. On the other hand, since such low signals are recorded, it is instructive to know how well the detector records small numbers of scattered photons. We evaluated the detector's capabilities in this regard by examining the distribution of photon counts recorded during exposure times for continuous and 2.56 µs burst-mode operations and comparing the observed distributions with expectations for scattering with a partially coherent X-ray beam.

The expected distribution of photon counts depends, for example, on the beam coherence, dynamics in the sample and the exposure time, and has been described previously for a variety of detectors and experiment configurations (Livet *et al.*, 2000; Gutt *et al.*, 2009; Hruszkewycz *et al.*, 2012; Li *et al.*, 2014; Wingert *et al.*, 2015; Verwohlt *et al.*, 2018). For a partially coherent beam, the probability for $k$ photons to be recorded in a pixel when the average count rate per pixel is $\bar{k}$ is given by the negative binomial distribution (Hruszkewycz *et al.*, 2012)

$$P(k) = \frac{\Gamma(k+M)}{\Gamma(M)\,\Gamma(k+1)} \left(1 + \frac{M}{\bar{k}}\right)^{-k} \left(1 + \frac{\bar{k}}{M}\right)^{-M}, \quad (4)$$

where $M$ is the number of coherent modes and $\Gamma$ is the gamma function. In the limit of large $M$ the probability reduces to the Poisson distribution: $P(k) = \bar{k}^k \exp(-\bar{k})/k!$. Other factors that affect the measured distributions are pixel-response dead-time, which is the time for the pixel electronics to recover after counting a photon, and the fact that the UFXC32k is a counting detector so any two-photon scattering events from a single bunch into a single pixel will be recorded as a single count. The pixel-response dead-time, $\tau_D$, of the UFXC32k has previously been measured to be as low as $\tau_D = 85$ ns (Grybos *et al.*, 2016) with near linear response to incoming photon fluxes to $\sim 10^6$ photons pixel$^{-1}$ s$^{-1}$. The maximum scattering signals in our measurements, around $10^4$ photons pixel$^{-1}$ s$^{-1}$, are well below this limit. Moreover, $\tau_D$ is much greater than the bunch separation (11 ns) suggesting that the source effectively appears continuous and the bunch structure is not important. These suggest, at first glance, that pixel-response dead-time need not be considered further and this is true for measurements of the average intensity (see below). On the other hand, measuring the contrast in a speckle pattern *via* speckle visibility depends sensitively on the relative distribution of 1 s and 2 s recorded in the detector during each integration time. Specifically, in the limit of weak scattering, Hruszkewycz *et al.* (2012) showed that

$$\beta = \frac{2P(2)\,[1 - P(1)]}{P(1)^2} - 1, \quad (5)$$

with $P(i)$ the probability of $i$ photons being recorded in a pixel during an exposure time.
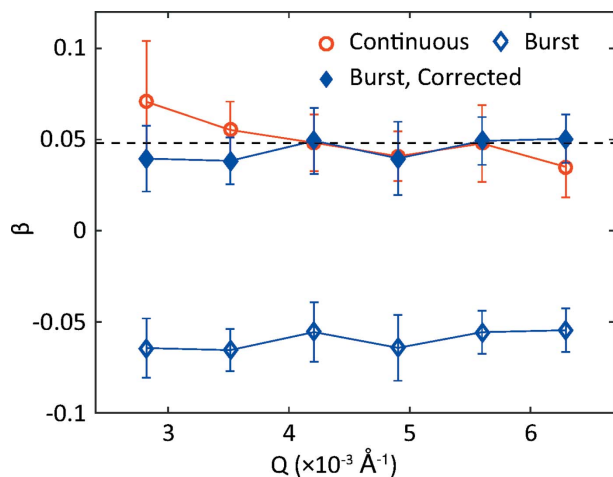
**Figure 7**
$\beta$ values determined by comparing the relative distribution of one- and two-photon events for 2.56 µs burst- (open diamonds) and continuous-mode data (open circles) acquired from the gold suspension. The solid diamonds are $\beta$ values calculated after correcting for pixel-response dead-time. The dashed black line indicates $\beta = \beta_1$ obtained from a static reference sample. The error bars are estimated from the standard deviation of $\beta$ in each $Q$ bin.



**Figure 8**
2.56 µs burst-mode measured probabilities (open symbols) for one- and two-photon counts (top and bottom panels, respectively) in a pixel as a function of the average intensity in a pixel. The solid and dashed lines are the calculated probabilities for fully coherent and fully incoherent (Poisson) scattering.

Fig. 7 shows the $\beta$ values calculated using equation (5) from the measured distribution of 1 s and 2 s for 2.56 µs burst- (open diamonds) and continuous-mode (open circles) data as a function of $Q$. Two features are immediately apparent. First, the $\beta$ values for continuous mode are roughly comparable with the amplitude of $\Delta g_2$ ($\beta_1$: dashed line) as one would expect since the exposure time of the detector is essentially fast enough to capture the short-time amplitude of $g_2$ (see Fig. 4). A more thorough comparison would require comparing $\beta$ determined *via* this visibility approach with smeared values of $\beta_1$ determined *via* a time autocorrelation. Details of this type of analysis are available and have been performed elsewhere (Bandyopadhyay *et al.*, 2005; Li *et al.*, 2014; Seaberg *et al.*, 2017; Verwohlt *et al.*, 2018). We have not pursued this approach here because with the limited integration times currently available from the UFXC32k (826 ns and 2.56 and 19.36 µs) we will not learn new information about the sample dynamics beyond what is available from measuring $g_2$. Second, and more striking, the $\beta$ values obtained in burst mode are negative indicating that the ratio of 2 s relative to 1 s is less than expected. This observation is made more evident in Fig. 8 that shows the measured probability of one- and two-photon occurrences (top and bottom panels, respectively) as a function of the average intensity in a pixel. The solid and dashed lines show the expected probabilities for fully coherent ($M = 1$) and fully incoherent (Poisson) scattering, respectively. The measured probability of 2 s is slightly below even that expected for the Poisson distribution.

We consider two origins for the relative lack of 2 s: (i) two-photon hits from a single bunch being recorded as a one-photon hit because the UFXC32k is a counting detector, and (ii) the pixel-response dead-time suppressing the registration of more than one hit (from different bunches) during an exposure. The probability of two-photon events from a single
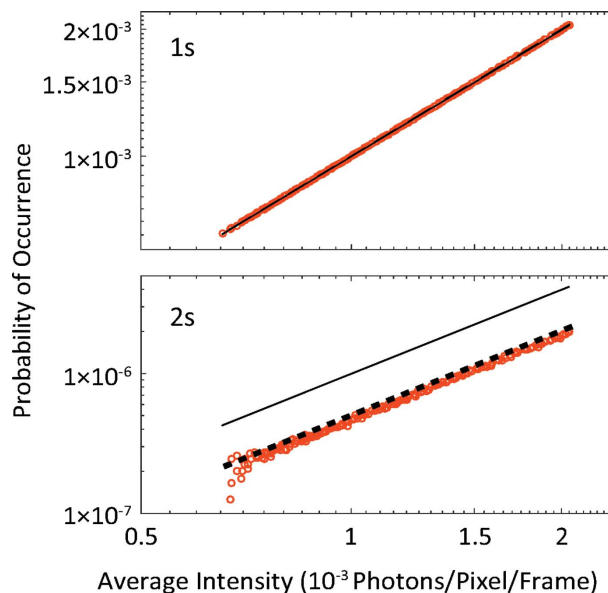
bunch is proportional to $P(1)^2$. This probability is considerably smaller than the probability for two 1 s from different bunches so is not a significant factor. With respect to pixel-response dead-time, as illustrated schematically in the bottom portion of Fig. 1(b), a photon hit (bold magenta signal) will preclude a second photon hit being counted if the photon arrivals are separated by a time gap shorter than the pixel-response dead-time (signals in the dashed yellow boxes). This is a more important effect for burst-mode because the relative error arising from this, $2\tau_D/t_e$ (Zhou, 2008), is much bigger.

To test this idea, we examined how the burst-mode $\beta$-values (Fig. 7) would change for different $\tau_D$. The solid diamonds in Fig. 7 are the $\beta$ values determined from the burst-mode data if the number of 2 s was increased to correct for $\tau_D = 130$ ns. Such a correction would result in a 10.2% increase in the number of 2 s. The pixel-response dead-time for the UFXC32k has previously been measured to be as low as 85 ns but, depending on details of how the detector has been configured, can be as high as 240 ns (Grybos *et al.*, 2016). The dead-time was not measured for the particular detector configuration that we used but, based on our knowledge of the configuration we used and how similar and different it is to other configurations that have been tested, we estimate $\tau_D = 125$–$150$ ns which encompasses our value of 130 ns.

To conclude this section we note that the photon-distribution effects we have been discussing do not affect either the measurement of $g_2$ determined by a time series of intensities (Figs. 4 and 5) or precise measurements of the time-average scattered intensity (Figs. 2 and 3). With respect to measuring time correlation functions with high fidelity, we note that $\tau_D$ affects measurements only when the sampling time is comparable with $\tau_D$ or the per-pixel count rate is high and

non-linearity occurs (Schätzel, 1986). In our study, the smallest sampling time is six times larger than our estimate for $\tau_D$ (130 ns) and the highest count rate, $10^4$ photons pixel$^{-1}$ s$^{-1}$, is 100 times smaller than where saturation non-linearity starts to occur (Grybos et al., 2016). With respect to time-average intensity measurements, we note that the one-photon count rates are far less than where saturation non-linearity occurs, while, for two photons, the dead-time leads to a 10.2% ($2\tau_D/t_e$) reduction in signal in the burst mode (and less in the continuous mode). The contribution of 2 s to the total intensity is less than 2% so the effect of $\tau_D$ on the total recorded intensity is 0.2% which is much smaller than the error bars in Fig. 4.

## 5. Conclusions

We have demonstrated greatly increased time resolution for multi-speckle XPCS by using the UFXC32k detector in a so-called hybrid mode that combines burst and continuous modes to achieve XPCS sampling times continuously spanning 826 ns to 52.8 s or nearly eight decades in delay time. By combining the $g_2$ values calculated from these modes, we have demonstrated sub-microsecond-resolved multi-speckle XPCS. We have also demonstrated the ability of the UFXC32k to faithfully record scattered X-rays at low count rates by comparing the probability of expected and measured photon counts and show that these results are consistent with $g_2$ measurements provided that pixel-response dead-time effects are included. On the one hand, our results demonstrate the need for PADs with increasingly smaller values of $\tau_D$. On the other hand, our results show that multi-speckle $g_2$ measurements continue to work well at very short delay times even at very low average signal levels. Our work makes progress toward a key requirement for fully utilizing anticipated MBA sources for XPCS, namely the need for XPCS-suitable area detectors to record scattered X-rays with high fidelity and at very high frame rates spanning a large dynamic range in time.

## References

Bandyopadhyay, R., Gittings, A. S., Suh, S. S., Dixon, P. K. & Durian, D. J. (2005). *Rev. Sci. Instrum.* **76**, 093110.

Becker, J., Bianco, L., Dinapoli, R., Göttlicher, P., Graafsma, H., Greiffenberg, D., Gronewald, M., Henrich, B. H., Hirsemann, H., Jack, S., Klanner, R., Klyuev, A., Krüger, H., Lange, S., Marras, A., Mozzanica, A., Schmitt, B., Schwandt, J., Sheviakov, I., Shi, X., Trunk, U., Zimmer, M. & Zhang, J. (2013). *J. Instrum.* **8**, C01042.

Becker, J., Gutt, C. & Graafsma, H. (2011). *J. Instrum.* **6**, P11005.

Broennimann, Ch., Eikenberry, E. F., Henrich, B., Horisberger, R., Huelsen, G., Pohl, E., Schmitt, B., Schulze-Briese, C., Suzuki, M., Tomizaki, T., Toyokawa, H. & Wagner, A. (2006). *J. Synchrotron Rad.* **13**, 120–130.

Burghardt, W. R., Sikorski, M., Sandy, A. R. & Narayanan, S. (2012). *Phys. Rev. E*, **85**, 021402.

Cipelletti, L. & Weitz, D. A. (1999). *Rev. Sci. Instrum.* **70**, 3214–3221.

Dierker, S. B., Pindak, R., Fleming, R. M., Robinson, I. K. & Berman, L. (1995). *Phys. Rev. Lett.* **75**, 449–452.

Eriksson, M., van der Veen, J. F. & Quitmann, C. (2014). *J. Synchrotron Rad.* **21**, 837–842.

Evenson, Z., Ruta, B., Hechler, S., Stolpe, M., Pineda, E., Gallino, I. & Busch, R. (2015). *Phys. Rev. Lett.* **115**, 175701.

Falus, P., Lurio, L. B. & Mochrie, S. G. J. (2006). *J. Synchrotron Rad.* **13**, 253–259.

Fluerasu, A., Moussaïd, A., Falus, P., Gleyzolle, H. & Madsen, A. (2008). *J. Synchrotron Rad.* **15**, 378–384.

Grybos, P., Kmon, P., Maj, P. & Szczygiel, R. (2016). *IEEE Trans. Nucl. Sci.* **63**, 1155–1161.

Gutt, C., Stadler, L. M., Duri, A., Autenrieth, T., Leupold, O., Chushkin, Y. & Grübel, G. (2009). *Opt. Express*, **17**, 55–61.

Hruszkewycz, S. O., Sutton, M., Fuoss, P. H., Adams, B., Rosenkranz, S., Ludwig, K. F. J., Roseker, W., Fritz, D., Cammarata, M., Zhu, D., Lee, S., Lemke, H., Gutt, C., Robert, A., Grübel, G. & Stephenson, G. B. (2012). *Phys. Rev. Lett.* **109**, 185502.

Inoue, I., Shinohara, Y., Watanabe, A. & Amemiya, Y. (2012). *Opt. Express*, **20**, 26878–26887.

Jakeman, E. (1973). *Photon Correlation and Light Beating Spectroscopy*, edited by H. Z. Cummins and E. R. Pike, pp. 75–149. New York: Plenum.

Johnson, I., Bergamaschi, A., Buitenhuis, J., Dinapoli, R., Greiffenberg, D., Henrich, B., Ikonen, T., Meier, G., Menzel, A., Mozzanica, A., Radicci, V., Satapathy, D. K., Schmitt, B. & Shi, X. (2012). *J. Synchrotron Rad.* **19**, 1001–1005.

Koziol, A., Bordessoule, M., Ciavardini, A., Dawiec, A., Da Silva, P., Desjardins, K., Grybos, P., Kanoute, B., Laulhe, C., Maj, P., Menneglier, C., Mercere, P., Orsini, F. & Szczygiel, R. (2018). *J. Synchrotron Rad.* **25**, 413–418.

Koziol, A. & Maj, P. (2018). *J. Instrum.* **13**, C02049.

Kraft, P., Bergamaschi, A., Broennimann, Ch., Dinapoli, R., Eikenberry, E. F., Henrich, B., Johnson, I., Mozzanica, A., Schlepütz, C. M., Willmott, P. R. & Schmitt, B. (2009). *J. Synchrotron Rad.* **16**, 368–375.

Leitner, M., Sepiol, B., Stadler, L. M., Pfau, B. & Vogl, G. (2009). *Nat. Mater.* **8**, 717–720.

Lhermitte, J. R., Rogers, M. C., Manet, S. & Sutton, M. (2017). *Rev. Sci. Instrum.* **88**, 015112.

Li, L., Kwaśniewski, P., Orsi, D., Wiegart, L., Cristofolini, L., Caronna, C. & Fluerasu, A. (2014). *J. Synchrotron Rad.* **21**, 1288–1295.

Livet, F., Bley, F., Ehrburger-Dolle, F., Morfin, I., Geissler, E. & Sutton, M. (2006). *J. Synchrotron Rad.* **13**, 453–458.

Livet, F., Bley, F., Mainville, J., Caudron, R., Mochrie, S. G. J., Geissler, E., Dolino, G., Abernathy, D., Grübel, G. & Sutton, M. (2000). *Nucl. Instrum. Methods Phys. Res. A*, **451**, 596–609.

Lumma, D., Lurio, L. B., Mochrie, S. G. J. & Sutton, M. (2000). *Rev. Sci. Instrum.* **71**, 3274–3289.

Magatti, D. & Ferri, F. (2001). *Appl. Opt.* **40**, 4011–4021.

# research papers

Malik, A., Sandy, A. R., Lurio, L. B., Stephenson, G. B., Mochrie, S. G. J., McNulty, I. & Sutton, M. (1998). *Phys. Rev. Lett.* **81**, 5832–5835.

Müller, L., Waldorf, M., Gutt, C., Grübel, G., Madsen, A., Finlayson, T. R. & Klemradt, U. (2011). *Phys. Rev. Lett.* **107**, 105701.

Nygård, K., Buitenhuis, J., Kagias, M., Jefimovs, K., Zontone, F. & Chushkin, Y. (2016). *Phys. Rev. Lett.* **116**, 167801.

Orsi, D., Cristofolini, L., Baldi, G. & Madsen, A. (2012). *Phys. Rev. Lett.* **108**, 105701.

Philipp, H. T., Tate, M. W., Purohit, P., Shanks, K. S., Weiss, J. T. & Gruner, S. M. (2016). *J. Synchrotron Rad.* **23**, 395–403.

Rieker, T., Hanprasopwattana, A., Datye, A. & Hubbard, P. (1999). *Langmuir*, **15**, 638–641.

Rogers, M. C., Chen, K., Andrzejewski, L., Narayanan, S., Ramakrishnan, S., Leheny, R. L. & Harden, J. L. (2014). *Phys. Rev. E*, **90**, 062310.

Sanborn, C., Ludwig, K. F., Rogers, M. C. & Sutton, M. (2011). *Phys. Rev. Lett.* **107**, 015702.

Schätzel, K. (1986). *Appl. Phys. B*, **41**, 95–102.

Schätzel, K. (1990). *Quantum Opt.* **2**, 287–305.

Schätzel, K. (1993). In *Dynamic Light Scattering: The Method and Some Applications*, edited by W. Brown. Oxford: Clarendon Press.

Schwandt, J., Fretwurst, E., Klanner, R., Poehlsen, T. & Zhang, J. (2013). *Nucl. Instrum. Methods Phys. Res. A*, **731**, 252–254.

Seaberg, M. H., Holladay, B., Lee, J. C. T., Sikorski, M., Reid, A. H., Montoya, S. A., Dakovski, G. L., Koralek, J. D., Coslovich, G., Moeller, S., Schlotter, W. F., Streubel, R., Kevan, S. D., Fischer, P., Fullerton, E. E., Turner, J. L., Decker, F. J., Sinha, S. K., Roy, S. & Turner, J. J. (2017). *Phys. Rev. Lett.* **119**, 067403.

Shinohara, Y., Watanabe, A., Kishimoto, H. & Amemiya, Y. (2013). *J. Synchrotron Rad.* **20**, 801–804.

Sutton, M., Laaziri, K., Livet, F. & Bley, F. (2003). *Opt. Express*, **11**, 2268–2277.

Verwohlt, J., Reiser, M., Randolph, L., Matic, A., Medina, L. A., Madsen, A., Sprung, M., Zozulya, A. & Gutt, C. (2018). *Phys. Rev. Lett.* **120**, 168001.

Vodnala, P., Karunaratne, N., Lurio, L., Thurston, G. M., Vega, M., Gaillard, E., Narayanan, S., Sandy, A., Zhang, Q., Dufresne, E. M., Foffi, G., Grybos, P., Kmon, P., Maj, P. & Szczygiel, R. (2018). *Phys. Rev. E*, **97**, 020601.

Walko, D. A., Arms, D. A. & Landahl, E. C. (2008). *J. Synchrotron Rad.* **15**, 612–617.

Wandersman, E., Chushkin, Y., Dubois, E., Dupuis, V., Robert, A. & Perzynski, R. (2015). *Soft Matter*, **11**, 7165–7170.

Westermeier, F., Pennicard, D., Hirsemann, H., Wagner, U. H., Rau, C., Graafsma, H., Schall, P., Paul Lettinga, M. & Struth, B. (2016). *Soft Matter*, **12**, 171–180.

Wingert, J., Singer, A. & Shpyrko, O. G. (2015). *J. Synchrotron Rad.* **22**, 1141–1146.

Wong, A. P. Y. & Wiltzius, P. (1993). *Rev. Sci. Instrum.* **64**, 2547–2549.

Zhang, Q., Bahadur, D., Dufresne, E. M., Grybos, P., Kmon, P., Leheny, R. L., Maj, P., Narayanan, S., Szczygiel, R., Ramakrishnan, S. & Sandy, A. (2017). *Phys. Rev. Lett.* **119**, 178006.

Zhang, Q., Dufresne, E. M., Grybos, P., Kmon, P., Maj, P., Narayanan, S., Deptuch, G. W., Szczygiel, R. & Sandy, A. (2016). *J. Synchrotron Rad.* **23**, 679–684.

Zhou, X. (2008). *A Practical Guide to Quantitative Finance Interviews*, 14th ed., p. 88. CreateSpace Publishers.